Investigation on nucleation of intergranular stress corrosion cracking in austenitic stainless steel by in situ strain measurement

Investigation on nucleation of intergranular stress corrosion cracking in austenitic stainless steel by *in situ* strain measurement

Tomoyuki Fujii[*1], Yoshikatsu Hisada[1], Keiichiro Tohgo[1], and Yoshinobu Shimamura[1]

[1] Department of Mechanical Engineering, Shizuoka University

3-5-1, Johoku, Naka-ku, Hamamatsu 432-8561, Japan

Corresponding author: Dr. T. Fujii

E-mail: fujii.tomoyuki@shizuoka.ac.jp

Tel & Fax: +81-53-478-1029

Abstract

This study evaluates the nucleation criterion for intergranular stress corrosion cracking (SCC) on a smooth surface of type 304 austenitic stainless steel from a mechanical viewpoint. SCC testing was conducted under a constant load, and microscopic strains on a smooth surface were measured *in situ* by the digital image correlation technique. The initiation period and site of intergranular cracks were estimated from the change in the microscopic strain distribution near grain boundaries (GBs), and the crack initiation was evaluated using strains at GBs just before cracking. As a result, the initiation of an intergranular crack could be characterized by evaluating only the maximum normal strain along the GB. The criterion for crack initiation was determined to be a maximum normal strain > 0.01 from the viewpoint of local strain.

Keywords: Stress corrosion cracking; Crack initiation; Stainless steel; Strain; Digital image correlation

1. Introduction

Structural integrity in chemical plants, power plants, etc. is assessed to ensure their safe use during long-time service. It has been reported that accidents are caused by the failure of structural components, by mechanisms such as fatigue, corrosion, stress corrosion cracking (SCC), and creep, and their remaining service life should be evaluated taking failure mechanisms into account. Among them, much attention has been paid to fatigue and SCC, because failures that occur from micro-cracks are difficult to detect by non-destructive inspection. Failures related to cracking are evaluated by studying crack initiation and crack propagation to estimate the service life of structural components. Techniques based on the mechanics of materials (stress- and strain-based approaches) are applied to evaluate the service life of smooth components [1-3], and techniques based on the fracture mechanics approach (stress intensity and *J* integral) are applied to evaluate the service life of flawed components [4-8]. In power plants, in order to evaluate the remaining service life of a component with a crack detected in periodic inspection, fracture mechanics approaches have been applied [9,10]. The time to crack initiation on a smooth surface, however, accounts for a large proportion of the total service life and should be considered in order to evaluate the total service life.

We have focused on evaluation of the service life of structural components influenced by SCC. It is well-known that SCC behaves in a hierarchical manner: the initiation, growth and coalescence of multiple micro-cracks, followed by macro-crack growth [11]. Hence, we developed a Monte Carlo simulation technique taking account of such multiple processes, from micro-crack initiation to macro-crack growth [12,13]. The technique considers the following three processes: micro-crack initiation, crack coalescence, and crack growth. Crack initiation is assumed to be a stochastic process, and the crack initiation period, site, and crack size are determined using random numbers. On the other hand, crack coalescence and growth are assumed to be deterministic processes, and these are dealt with based on a fracture mechanics approach. In this simulation, the size of an initiated crack is determined based on the microstructure of the material, and a crack is assumed to be initiated along a whole grain boundary (GB). The elementary process of crack initiation on a smooth surface of the material is not considered, and a criterion for crack initiation should be formulated to improve the simulation.

SCC occurs under the conjoint action of material, aggressive environment, and mechanical forces, and the crack initiation criteria should be investigated from these influencing factors. From the environmental viewpoint, the influence of temperature and ionic impurities on crack initiation behavior was discussed [14-16]. From the material viewpoint, the susceptibility to SCC has been investigated using GB structures and networks measured by the electron backscatter diffraction (EBSD) technique. Gertsman and Bruemmer [17] tried to clarify the initiation of intergranular cracks and pointed out that it is impossible to discuss crack initiation using only the GB structures based on the coincidence site lattice (CSL) model. Rahimi and Marrow [18] and Fujii et al. [19] pointed out that GB structure and grain size significantly influenced the susceptibility to intergranular SCC in type 304 stainless steel. Rahimi et al. [20] and Liu et al. [21] investigated the influence of GB network on SCC susceptibility in type 304 stainless steel and type 316 stainless steel, respectively, and demonstrated that SCC resistance could be improved by increasing the fraction of twin ($\Sigma 3$) boundaries. From the mechanical viewpoint, some approaches have been applied to characterize the nucleation of SCC. West and Was [22] investigated the initiation of an intergranular crack based on normal stress acting at a GB. To calculate the normal stress at a GB, they proposed a simple technique, the Schmid-modified grain boundary stress (SMGBS) model, based on only the Schmid factors for two grains neighboring the GB. They pointed out that an intergranular crack occurs at a highly normal-stressed GB. Stratulat et al. [23], Zhang et al. [24] and Fujii et al. [19] also discussed crack initiation in austenitic stainless steel using the SMGBS model, and reached conclusions similar to those in Ref. 22. Johnson et al. [25] measured the microscopic stress using high-resolution EBSD technique, and developed a criterion for crack initiation in irradiated Fe-based alloys using normal stress acting at a GB. On the other hand, West et al. [26,27] investigated the influence of local strain around a GB on crack initiation. McIntyre et al. [28] and Ulaganathan et al. [29] also evaluated the relationship between SCC behavior and local strains at GBs in Ni-based alloy and copper-zinc alloy, respectively. They pointed out that the local strains play an important role for crack initiation and propagation. So far, the applicability of stress-based approach and/or strain-based approach to stress corrosion crack initiation is still controversial.

We focused on the strain-based approach to characterize stress corrosion crack initiation and used the digital image correlation (DIC) technique to measure local strains at GBs because the strains

could be directly measured [30]. The results showed that crack initiation tended to be characterized by the normal strain at a GB, and a GB with only slight tensile normal strain might be cracked, which is somewhat questionable. In the study, crack initiation was characterized using local strains measured before SCC testing. The strains, however, redistribute during testing due to time-dependent deformations such as creep and cracking, and this effect on crack initiation is ignored. Hence, crack initiation must be characterized using mechanical quantities just before crack initiation at a GB. To measure strain *in situ* in a corrosive environment, the DIC technique is quite useful. Rahimi et al. [20], Stratulat et al. [23], and Bolivar et al. [31] applied DIC to detect SCC nucleation. Aswad and Marrow [32] also applied DIC to investigate intergranular crack initiation, but they did not evaluate the relationship between crack initiation and local strains. It is expected that the time to crack initiation can be evaluated if a strain-based approach to characterize stress corrosion crack initiation is established.

This study proposed a criterion of intergranular stress corrosion crack initiation on sensitized austenitic stainless steel from a mechanical viewpoint. SCC testing was conducted, and microscopic strains on a smooth surface of a specimen subjected to constant loading were measured *in situ* using DIC. The crack initiation at GBs was investigated by comparing the local strains at cracked and uncracked GBs.

2. Experimental procedure

This section describes the procedures of specimen preparation and SCC testing used in this study, some of which are similar to those used in our previous studies [19,30]. See the previous reports for details on the procedures.

2.1 Material and specimen

This study used type 304 austenitic stainless steel, whose chemical composition and mechanical properties are listed in Table 1. The steel was heat-treated at 1100°C for 1 h for solutionizing, and then at 700°C for 2 h and 500°C for 24 h for sensitizing. The sensitization ratio of the steel was 29.3%, which was measured by the electrochemical reactivation testing technique (Japanese Industry Standard (JIS) G 0580). Tensile specimens were made from the heat-treated bulk

steel by wire electrical discharge machining (EDM). Figure 1 shows the dimensions of a tensile specimen, which has a 1×1 mm rectangular observation area. All surfaces were ground with emery paper up to #2000 to remove the altered layer created by wire EDM. Then, only the observation area was mirror-polished with diamond paste with a 0.3 μm particle size. The specimen coordinate system was set as the loading direction (*x*), normal to the loading direction (*y*), and normal to the specimen surface (*z*).

The DIC technique was applied to characterize the initiation of intergranular corrosion cracks based on strains at a GB. The strains were calculated using the open-source software Ncorr [33], and the conditions of the DIC technique are shown in Table 2. A random pattern needs to be formed on a specimen surface to apply the DIC technique, and the pattern has been generally created by use of black and white paint [34,35]. Such a pattern, however, protects against SCC occurrence because the paint behaves as an insulating coating, and this technique is inappropriate for applying *in situ* strain measurement during SCC testing. Hence, we created a random pattern on the specimen surface using an etch pit technique proposed by Stratulat et al. [23]. The observation area was etched in a mixed acid solution of 92% acetic acid and 8% perchloric acid at 13 V for 35 s using a constant power source (POLIPOWER, Marumoto Struers K.K.). Figure 2 shows an example of the etched surface of the specimen, and etch pits and IGC grooves are observed. The etch pits were formed at the sites of lattice defects in the grains, and the corrosion grooves were formed at GBs with high susceptibility to IGC, such as high-angle random boundaries [36]. Although corrosion grooves were not desired during the conducting of SCC testing and application of DIC for strain measurement, it was impossible to create a random pattern consisting of only etch pits without corrosion grooves. Note that it may be impossible to observe SCC behavior *in situ* using an etched specimen, because SCC may occur at corrosion grooves formed at the GBs with high IGC susceptibility. Appendixes A and B explain the measurement of strain by DIC using this random pattern in detail, and the influence of the geometry of corrosion grooves on strain distribution, respectively.

2.2 SCC testing apparatus

Figure 3 illustrates a schematic of the laboratory-made tensile testing apparatus. The specimen is inserted inside a plastic tube, and constant tensile loading can be applied with a

compressive spring. Prior to testing, all surfaces of the specimen except for its observation area are coated with plastic. Due to the tube and plastic coating, only the observation area is immersed in a corrosive solution. This specimen setting leads to SCC occurrence being inhibited outside of the observation area, and surface changes, such as surface deformation and SCC occurrence, can be observed *in situ* through a glass plate with an OM (MS-Z420. Asahi Kogaku Manuf. Co., Ltd.). During testing, the applied strain is measured by a strain gauge, which is attached to the back surface of the observation area.

2.3 Experimental

After creating the random pattern within the observation area, a plastic coating was formed on all the specimen surfaces except for the observation area, and then the specimen was placed in the testing apparatus. A corrosive solution, which was a 1% tetrathionate solution with a pH of 3.0, was poured into the plastic tube. A tensile load was applied corresponding to an initial strain of 1%, measured with the strain gauge attached to the back surface of the observation area. During testing, images of the observation area were taken every 0.5 h, and the distributions of strains were calculated by DIC. SCC testing was performed at room temperature (RT), and terminated after a testing time of 24 h. After testing, the plastic coating was removed with acetone, and the cracked surface was observed by scanning electron microscopy (SEM, VE-9800, Keyence). The relationship between microscopic strains at GBs and crack sites was investigated. Three specimens were tested in the same experimental conditions.

3. Results and discussion

3.1 Crack profile and strain distributions

Figure 4 shows images of the observation area during testing. As explained above, although changes in the random pattern on the surface are observed, SCC behavior, such as crack initiation and growth, cannot be observed. Figure 5 shows SEM micrographs of the specimen, which correspond to the image shown in Fig. 4(b). Several cracks are observed at only the IGC groove bottoms, and tend to be preferentially initiated at the GBs normal to the loading direction. From a viewpoint of influence of GB structure on crack initiation, the cracks may be initiated at only the

GBs with high IGC susceptibility because IGC groove is formed along GBs with high IGC susceptibility [36]. The crystal orientation in the vicinity of GBs could not be measured using EBSD technique due to the IGC groove, and the influence of GB structure on crack initiation was not further discussed. This was previously discussed in detail using EBSD technique by several researchers, as explained in the introduction.

Figures 6 and 7 show the distributions of strains ε_{xx}, ε_{yy}, and $\gamma_{xy}/2$ on the observation area at 0 h and 12 h, respectively. Although a uniform strain was macroscopically applied, microscopic strains were distributed heterogeneously due to anisotropic grain deformation, such as slip deformation. The strain distributions changed slightly as the loading time proceeded. These strain changes would be caused by creep and cracking: it is well known that creep deformation occurs at RT in austenitic stainless steels [37], and crack initiation and growth result in the redistribution of microscopic strains around a crack site. Note that the surface roughness increased as time proceeded, and the area in which the strains could not be calculated by DIC expanded.

The crack initiation period could not be detected by *in situ* observation, as mentioned above. Hence, the period was estimated from the viewpoint of strain distribution. If a crack is initiated at a GB, the following changes in strain distribution near the GB occur: strains along the GB are decreased due to elastic unloading at crack planes, while strains near the GB ends are increased due to the stress/strain concentration, because the GB ends become crack tips. Figure 8 shows an example of the strain distribution ε_{xx} around the GB shown in Fig. 5(b) at the immersion times of 9 h and 10 h. Although little change in strain distribution along the GB is observed, the strain remarkably increases at the upper GB end. The crack seemed to be initiated between the immersion times of 9 h and 10 h. In similar fashion, the initiation periods of all cracks observed by SEM were determined.

3.2 Criterion for crack initiation

Normal and shear strains along a GB were calculated to characterize crack initiation,

$$\varepsilon_\theta = \frac{\varepsilon_{xx}+\varepsilon_{yy}}{2} + \frac{\varepsilon_{xx}-\varepsilon_{yy}}{2}\cos 2\theta - \frac{\gamma_{xy}}{2}\sin 2\theta, \tag{1a}$$

$$\frac{\gamma_\theta}{2} = \frac{\varepsilon_{xx}-\varepsilon_{yy}}{2}\sin 2\theta + \frac{\gamma_{xy}}{2}\cos 2\theta, \tag{1b}$$

where θ is the angle between a GB and a plane normal to the tensile direction, and ε_θ and γ_θ are normal and shear strains along a GB, respectively. Each GB was assumed to be straight for the sake of simplicity. Figure 9 shows the normal and shear strain distributions along the GB shown in Fig. 8 at the immersion time of 9 h. The strains at sites where they could not be measured were estimated by interpolation from the strains at neighboring sites. As mentioned in Sec. 3.1, normal and shear strains were distributed heterogeneously. In our previous study [30], a crack was found to occur at a site in a GB where the normal strain is high, and then grow along the whole GB. In this study, however, we were not able to observe any crack initiation behavior in detail. Assuming that the crack initiation behavior was similar to the results of the previous study, crack initiation was characterized using the maximum normal and shear strains. Figure 10 shows the histograms of the number of GBs versus maximum normal and shear strains at cracked GBs and all GBs (cracked and uncracked GBs). The numbers of cracked, uncracked and all GBs are denoted by n_c, n_{unc}, and n_{all} ($=n_c+n_{unc}$), respectively. For cracked GBs, the maximum strains at 11 cracked GBs in total just before crack initiation were used. For uncracked GBs, we selected 35 uncracked GBs at random, and their normal and shear strains at 24 h were used. For characterization using maximum normal strain ε_{max}, although the histogram of all GBs was bell-shaped, that of the cracked GBs had a threshold at the maximum normal strain ε_{max} of 0.01. Only the GBs subjected to greater than the threshold strain ($\varepsilon_{max} > 0.01$) would be cracked. The average values of maximum normal strains for cracked and all GBs were 0.034 and 0.019, respectively. On the other hand, for characterization using the maximum shear strain $\gamma_{max}/2$, the shapes of both histograms were approximately bell-shaped. The average values of maximum shear strains for cracked and all GBs were 0.020 and 0.023, respectively, which are almost the same. Consequently, the initiation of an intergranular stress corrosion crack is affected by only the normal strain from the viewpoint of strain distribution, and it would be possible to characterize this using the maximum normal strain ε_{max} along a GB.

Figure 11(a) shows a histogram of the probability of cracked GBs versus maximum normal strain ε_{max}, which is defined as the ratio of the number of cracked GBs to the total number of GBs, n_c/n_{all}. Although no GBs were cracked when $\varepsilon_{max} < 0.01$, intergranular cracks tended to be initiated when $\varepsilon_{max} > 0.01$. This result suggested that the criterion for crack initiation is a maximum normal strain of 0.01 at a GB. Note that the probability of crack initiation n_c/n_{all} was overestimated, because

the number of uncracked GBs n_{unc} within the observation area is actually larger than the number used, due to the random selection of uncracked GBs in this experiment.

We plotted the relationship between n_c/n_{all} versus ε_{max} without taking strain redistribution into account, as shown in Fig. 11(b). The previous results concluded that the probability increased with increasing ε_{max} when $\varepsilon_{max} > 0$, while no GBs were cracked when $\varepsilon_{max} < 0$. This means that the crack initiation criterion (threshold strain) at a GB was $\varepsilon_{max} = 0$, and this is somewhat questionable because this implies that a crack may be initiated at any GB subjected to a small amount of tension. In this evaluation, we characterized the crack initiation using the maximum normal strain ε_{max} at GBs measured at the beginning of SCC testing, and this result would be caused from the lack of consideration of the redistribution of strains due to creep and cracking. As shown in Figs. 6 and 7, the strain distributions actually change as time proceeds. Even if strains at a GB are low at the beginning of testing, the strains may become higher during testing due to creep and cracking: the strain condition for crack initiation may be underestimated. Hence, the criterion proposed in this study is reasonably effective, because the strain state just before cracking is considered.

In this criterion, the threshold strain was determined as $\varepsilon_{max} = 0.01$, but some GBs subjected to higher normal strain were uncracked. Johnson et al. [25] also successfully determined the threshold stress acting on GBs for SCC nucleation in irradiated steel. Similar to our study, however, some GBs subjected to normal stress higher than the threshold stress were also uncracked. These criteria were developed from only the mechanical viewpoint, but other factors such as electro-chemistry and reaction formation near GBs must influence SCC behavior. In this study, although SCC occurred at GBs with high IGC susceptibility, the influence of IGC susceptibility on crack initiation was ignored. More investigation is needed to establish a criterion taking account of such influencing factors.

4. Conclusion

SCC testing was conducted on sensitized type 304 austenitic stainless steel in a tetrathionate solution, and microscopic strains were measured during testing *in situ*. SCC nucleation on a smooth surface was discussed on the basis of strains at GBs just before cracking. The results indicated that stress corrosion cracks preferentially occur at GBs with higher maximum normal strain. The

initiation of stress corrosion cracking can be characterized only by the maximum normal strain, not the maximum shear strain. The criterion for crack initiation along a GB was determined to be a maximum normal strain $\varepsilon_{max} > 0.01$ from a mechanical viewpoint.

Appendix A

This section demonstrates the accuracy of strains measured by the DIC technique used in this study. We created a random pattern on a smooth specimen surface by the etch pit technique, as shown in Fig. 2. As mentioned in Sec. 3, the etch pits were randomly formed in grains and a corrosion groove was formed at GBs. The tensile testing shown in Fig. A.1 was preliminarily conducted in the corrosive solution, and the accuracy of the strains measured by this technique was evaluated. A random pattern with an area of 1×1 mm was formed on the upper surface, and strain gauges with a length of 1 mm were attached to the upper and lower surfaces of the specimen. Note that the random pattern area was set as the gauge size. It is expected that the average value ε_{xx}^{ave} of strain ε_{xx} measured by DIC is equal to the strain measured by a strain gauge attached to the upper specimen surface ε^{u} when the stain measured by DIC is accurate. Figure A.2 shows a stress-strain curve obtained using the tensile testing apparatus. The horizontal axis represents the applied strain ε^{app}, which is the average strain measured with the strain gauges at the upper and lower surfaces (ε^{u} and ε^{l}). During testing, tension was intermittently loaded, and images of the observation area were taken at strain increments of 0.2%.

Figure A.3 shows the error $\varepsilon_{xx}^{ave} / \varepsilon^{u}$ as a function of the strain ε^{u}. When the applied strain was small, the average strain obtained by DIC was not comparable to the strain obtained by the strain gauge. As the strain increased, the average strain measured by DIC approached the strain measured by the strain gauge. The difference between them was less than 10% when the applied strain was greater than 0.6%. Hence, the strains measured by DIC in this study were accurate because we used an initially applied strain of 1.0%. Note that this result is almost the same as in our previous experiment [30] in which micro-sized drops of silicone oil were used as a random pattern.

Appendix B

The DIC technique calculates strains on a surface on the basis of the movement and deformation of a random pattern. In this study, the random pattern consisted of micro-sized dimples and grooves, which were very shallow, as shown in Fig. B.1. We used the dimples and grooves as a random pattern, and the strain concentration near their bottoms was ignored. This is understood from the fact that the average strain in the loading direction measured by DIC agrees with the strain measured by strain gauge, as shown in Appendix A. On the other hand, SCC nucleation may be influenced by the local strain.

In this section, the strain concentration at a shallow groove on a smooth surface is evaluated. When a corrosion groove is parallel to the loading direction, there is no stress concentration. As a corrosion groove becomes inclined to the loading direction, strain concentration occurs at the groove bottom. Then, the strain concentration is the highest when the corrosion groove is normal to the loading direction. Hence, for the sake of simplicity, only the worst case, in which a corrosion groove is normal to the loading direction, is investigated: a two-dimensional problem of a single side notch in a semi-infinite plate under tension is discussed. Moreover, the plate is assumed to be made of a homogeneous isotropic material, and the influences of material anisotropy and GB (an interface between dissimilar materials) on stress/strain distributions are ignored. The following should be noted: in an elastic body, the stress concentration and strain concentration factors are the same, and these are referred to K_{T}. The value of K_{T} can be found in some handbooks. On the other hand, in an elastoplastically deformed body, the strain concentration factor K_{ε} becomes larger that the stress concentration factor K_{σ} because stress relaxation occurs due to plastic deformation. We determined the strain concentration factor K_{ε} by Neuber's rule and the stress-strain curve of the steel [38,39]:

$$K_{\mathrm{T}}^2 = K_{\varepsilon} K_{\sigma}, \tag{B.1}$$

$$K_{\varepsilon} = \frac{\varepsilon_{\max}}{\varepsilon_n}, \ K_{\sigma} = \frac{\sigma_{\max}}{\sigma_n}, \tag{B.2}$$

where $\varepsilon_{\max}$ and ε_{n} are the maximum strain at a notch root and nominal strain, respectively, and $\sigma_{\max}$ and σ_{n} are the maximum stress at a notch root and nominal stress, respectively.

We observed the shapes of corrosion grooves by cutting the specimen with a random pattern, and the depth and width of corrosion grooves were measured. Table B.1 shows a summary of the groove geometry, elastic stress/strain concentration factor K_{T}, and plastic strain concentration factor

K_ε. Note that the value of K_T was calculated using the simple method proposed by Takase et al. [40] As a result, the value of K_ε is 4.7, which is fairly large. Hence, the strain concentration of the random pattern used in this study ranged from 1 to 4.7, which depends on the directions of loading and the groove. The influence of the strain concentration on SCC nucleation remains to be clarified, and more investigations are needed on this topic.

Acknowledgments

The authors would like to thank Dr. K. Nakazawa for technical discussions about the surface observations in Appendix B. This work was supported by the SUZUKI FOUNDATION in Japan.

References

[1] K.N. Smith, T. Topper, and P. Watson, A stress-strain function for the fatigue of metals, *Journal of Materials*, Vol. 5(1970), pp. 767-778.

[2] M. Mayuzumi, T. Arai, and K. Hide, Chloride Induced Stress Corrosion Cracking of Type 304 and 304L Stainless Steels in Air, *Zairyo-to-Kankyo*, Vol. 52(2003), pp. 166-177.

[3] R. Nishimura, Characterization and perspective of stress corrosion cracking of austenitic stainless steels (type 304 and type 316) in acid solutions using constant load method, *Corrosion Science*, Vol. 49 (2007), pp. 81-91.

[4] W. Schütz, The prediction of fatigue life in the crack initiation and propagation stages - a state of the art survey, *Engineering Fracture Mechanics*, Vol. 11 (1979), pp.405-421.

[5] I. Milne, R.O. Ritchie, and B. Karihaloo (Eds.), Comprehensive Structural Integrity, *Elsevier Science Ltd.*, 2003, pp. 41-128.

[6] H. Leinonen, Stress corrosion cracking and life prediction evaluation of austenitic stainless steels in calcium chloride solution, *Corrosion*, Vol. 52 (1996), pp. 337-346.

[7] P.L. Andresen and F.P. Ford, Life Prediction by mechanistic modeling and system monitoring of environmental cracking of iron and nickel alloys in aqueous systems, *Materials Science and Engineering: A*, Vol. 103 (1988), pp. 167-184.

[8] S. Uchida, Y. Chimi. S Kasahara, S. Hanawa, H. Okada, M. Naitoh, M. Kojima, H. Kikura, and D.H. Lister, Improvement of plant reliability based on combining of prediction and

inspection of crack growth due to intergranular stress corrosion cracking, *Nuclear Engineering and Design*, Vol. 341 (2019), pp. 112-123.

[9] ASME, Boiler and Pressure Vessel Code Section XI 2003 Addenda, ASME, New York (2003)

[10] JSME, Fitness-For-Service Code S NA1-2004, JSME, Tokyo (2004).

[11] M. Akashi and T. Kawamoto, Intergranular stress corrosion crack propagation behavior of sensitized stainless steels in high temperature pure water, *Boshoku Gijyutsu*, Vol. 32 (1983), 9-15.

[12] K. Tohgo, H. Suzuki, Y. Shimamura, G. Nakayama, and T. Hirano, Monte Carlo simulation of stress corrosion cracking on a smooth surface of sensitized stainless steel type 304, *Corrosion Science*, Vol. 51 (2009), pp. 2208-2217.

[13] T. Fujii, K. Tohgo, A. Kenmochi, and Y. Shimamura, Experimental and numerical investigation of stress corrosion cracking of sensitized type 304 stainless steel under high-temperature and high-purity water, *Corrosion Science*, Vol. 97 (2015), pp.139-149.

[14] W.E. Ruther, W.K. Soppet, T.F. Kassner, Effect of temperature and ionic impurities at very low concentrations on stress corrosion cracking of AISI 304 stainless steel, *Corrosion*, Vol. 44 (1988), pp. 791-799.

[15] S. Zhang, T. Shibata, and T. Haruna, Contribution of solution pH and buffer capacity to suppress intergranular stress corrosion cracking of sensitized type 304 stainless steel at 95°C, *Corrosion*, Vol. 55 (1999), pp. 462-468.

[16] S. Zhang, T. Shibata, and T. Haruna, Inhibition effect of metal cations to intergranular stress corrosion cracking of sensitized type 304 stainless steel, *Corrosion Science*, Vol. 47 (2005), pp. 1049-1061.

[17] V. Y. Gertsman and S. M. Bruemmer, Study of grain boundary character along intergranular stress corrosion crack paths in austenitic alloys, *Acta Materialia*, Vol. 49 (2001), pp. 1589-1598.

[18] S. Rahimi and T.J. Marrow, Effects of orientation, stress and exposure time on short intergranular stress corrosion crack behaviour in sensitised type 304 austenitic stainless steel, *Fatigue & Fracture of Engineering Materials & Structures*, Vol. 35 (2011), pp. 359-373.

[19] T. Fujii, K. Tohgo, Y. Mori, Y. Miura, and Y. Shimamura, Crystallographic and mechanical investigation of intergranular stress corrosion crack initiation in austenitic stainless steel, *Materials Science & Engineering: A*, Vol. 751 (2019), pp. 160-170.

[20] S. Rahimi, D.L. Engelberg, J.A. Duff, and T.J. Marrow, *In situ* observation of intergranular crack nucleation in a grain boundary controlled austenitic stainless steel, *Journal of Microscopy*, Vol. 233 (2009), pp. 423-431.

[21] T. Liu, S. Xia, Q. Bai, B. Zhou, Y. Lu, and T. Shoji, Evaluation of Grain Boundary Network and Improvement of Intergranular Cracking Resistance in 316L Stainless Steel after Grain Boundary Engineering, *Materials* ,Vol. 12 (2019), 242.

[22] E.A. West and G.S. Was, A model for the normal stress dependence of intergranular cracking of irradiated 316L stainless steel in supercritical water, *Journal of Nuclear Materials*, Vol. 408 (2011) , pp. 142-152.

[23] A. Stratulat, J.A. Duff, and T.J. Marrow, Grain boundary structure and intergranular stress corrosion crack initiation in high temperature water of a thermally sensitised austenitic stainless steel, observed in situ, *Corrosion Science*, Vol.85 (2014), pp. 428-435.

[24] Z. Zhang, S. Xia. Q. Bai. T. Liu. H. Li. B. Zhou, L. Wang, and W. Ma, Effects of 3-D grain boundary geometrical angles and the net normal stress on intergranular stress corrosion cracking initiation in a 316 stainless steel, *Materials Science and Engineering A*, Vol. 765 (2019), 138277.

[25] D.C. Johnson, B. Kuhr, D. Farkas, and G.S. Was, Quantitative linkage between the stress at dislocation channel - Grain boundary interaction sites and irradiation assisted stress corrosion crack initiation, *Acta Materialia*, Vol. 170 (2019), pp. 166-175.

[26] E.A West, M.D. McMurtrey, Z. Jiao, and G.S. Was, Role of localized deformation in irradiation-assisted stress corrosion cracking initiation, *Metallurgical and Materials Transactions A*, Vol. 43 (2012), pp. 136-146,

[27] E.A. West, and G.S. Was, Strain incompatibilities and their role in intergranular cracking of irradiated 316L stainless steel, *Journal of Nuclear Materials*, Vol. 441 (2013) , pp. 623-632.

[28] N.S. McIntyre, J. Ulaganathan, T.Simpson, J. Qin, N.Sherry, A.G. Carcea, R.C. Newman, M. Kunz, and N. Tamura, Microscopic Cracking on Flat Alloy 600 Surfaces following

Accelerated Caustic Corrosion: Mapping of Strains and Microstructure during the Corrosion Process, *Corrosion*, Vol. 71 (2014), pp. 65-70.

[29] J. Ulaganathan and R.C. Newman, The role of local strains from prior cold work on stress corrosion cracking of α-brass in Mattsson's solution, *Materials Characterization*, Vol. 92 (2014), pp. 127-137.

[30] T. Fujii, R. Yamakawa, K. Tohgo, and Y. Shimamura, Strain-based approach to investigate intergranular stress corrosion crack initiation on a smooth surface of austenitic stainless steel, *Materials Science and Engineering: A*, Vol. 756 (2019), pp. 518-527.

[31] J. Bolivar, M. Fregonese, J. Rethore, C. Duret-Thual, and P. Combrade, Evaluation of multiple stress corrosion crack interactions by in-situ digital image correlation, *Corrosion Science*, Vol. 128 (2017), pp. 120-129.

[32] M.A Aswad and T.J. Marrow, Intergranular crack nuclei in polycrystalline alumina, *Engineering Fracture Mechanics*, Vol. 95 (2012), pp. 29-36.

[33] J. Blaber, B. Adair, and A. Antoniou, Ncorr: Open-Source 2D Digital Image Correlation Matlab Software, *Experimental Mechanics*, Vol. 55 (2015), pp. 1105-1122.

[34] B. Pan, K. Qian, H. Xie, and A. Asundi, Two-dimensional digital image correlation for in-plane displacement and strain measurement: a review, *Measurement Science and Technology*, Vol. 20(6) (2009), 062001.

[35] T.A. Berfield, J.K. Patel, R.G. Shimmin, P.V. Braun, J. Lambros, and N.R. Sottos, Micro- and nanoscale deformation measurement of surface and internal planes via digital image correlation, *Experimental Mechanics*, Vol. 47 (2007), pp. 51-61.

[36] T. Fujii, K. Tohgo, Y. Mori, and Y. Shimamura, Crystallography of intergranular corrosion in sensitized austenitic stainless steel, *Materials Characterization*, Vol. 144 (2018), pp.219-226.

[37] M. Tendo, T. Takeshita, T. Nakazawa, H. Kimura, and H. Abo, Room temperature creep behavior of stainless steels, *Tetsu-to-Hagane*, Vol. 79 (1993), pp. 98-104.

[38] H. Neuber, Theory of stress concentration for shear-strained prismatical bodies with arbitrary nonlinear stress-strain law, *Transactions of the ASME, Journal of Applied Mechancis*, Vol. 28 (1961), pp. 544-550.

[39] ASME, Boiler & Pressure Vessel Code Case, Section III, Division 1 NH (2003) ASME.

[40] Y. Takase, N.A. Noda, Y. Gao, and T. Takemoto, Stress Concentration Formula Useful for Any Dimensions of Notches -Effect of Notch Opening Angle on the Stress Concentration Factor-, *Journal of the Society of Materials Science, Japan*, Vol. 52 (2003), pp. 795-800.

Figures

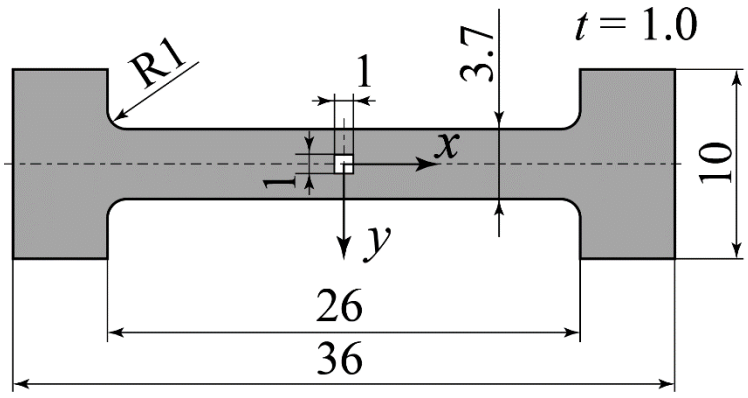

Fig. 1 Dimensions of a tensile specimen.

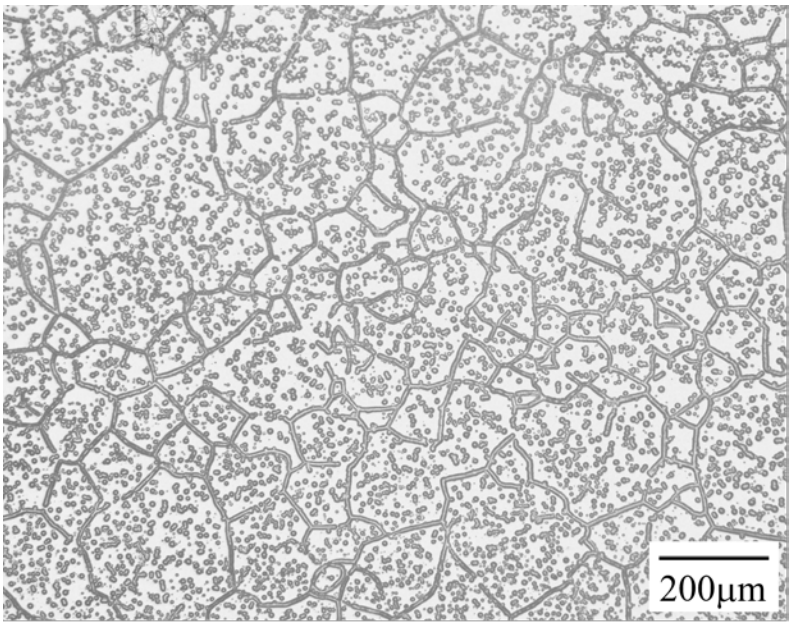

Fig. 2 Random pattern on a smooth surface.

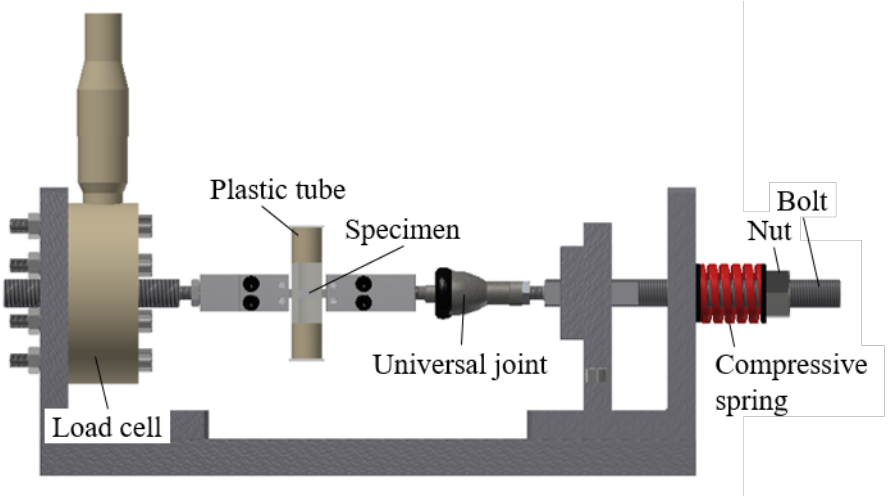

(a) Schematic illustration of the constant load testing apparatus.

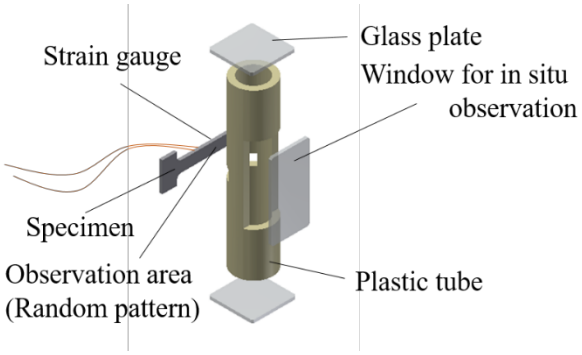

(b) Details of specimen mounting.

Fig. 3 Setup for constant-load (SCC) testing.

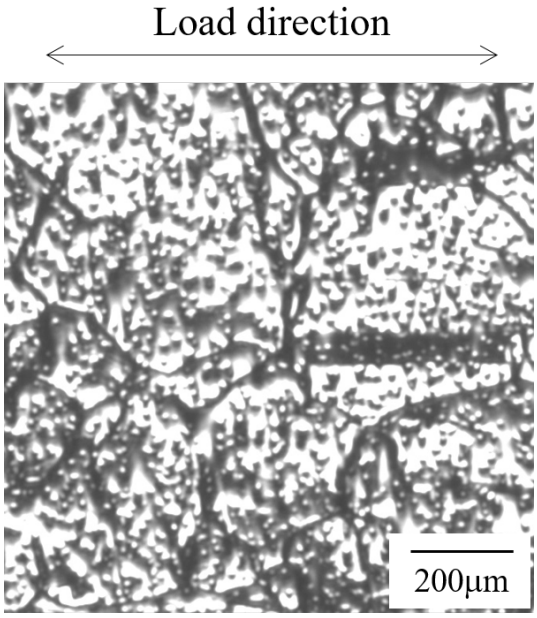

(a) 0 h

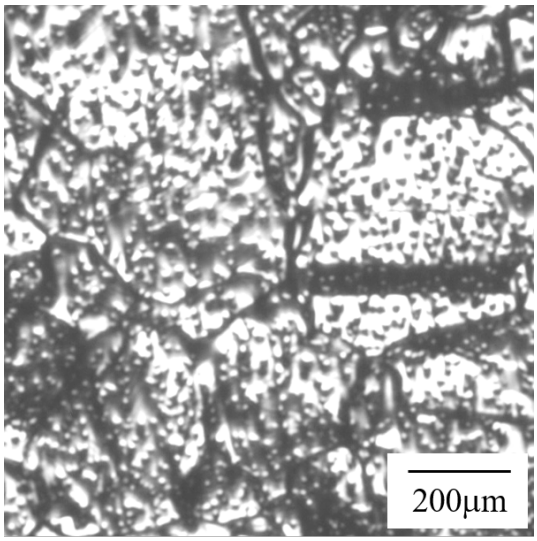

(b) 24 h

Fig. 4 *In situ* observation during testing (tensile strain of 1%).

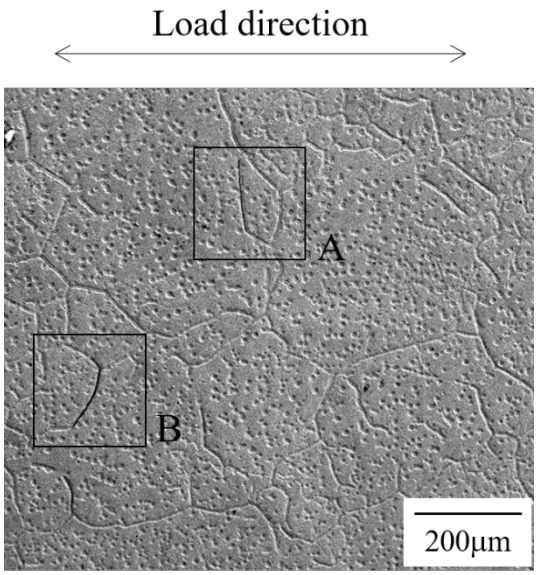

(a) Overall view

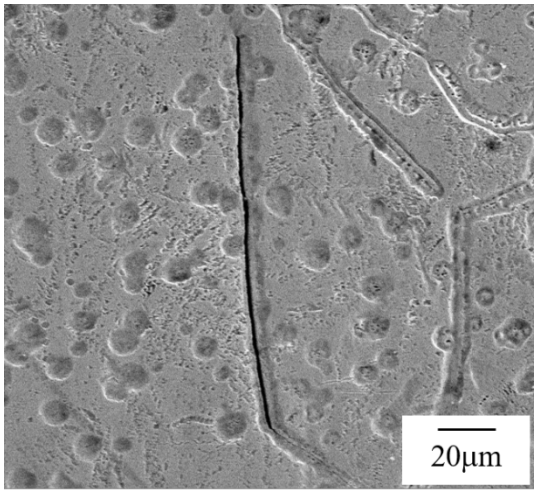

(b) Expansion of part A in panel (a)

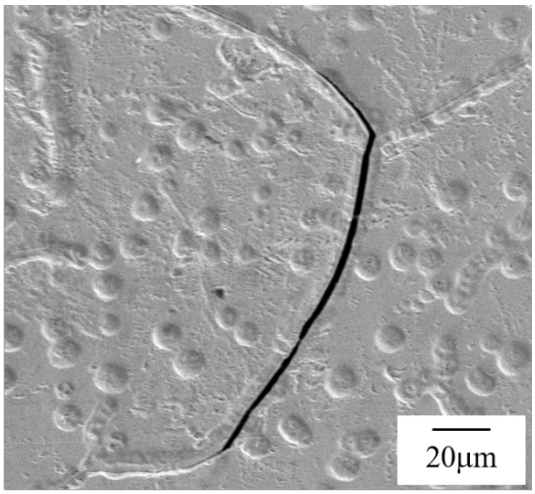

(c) Expansion of part B in panel (a)

Fig. 5 SEM micrographs of the specimen after testing.

Figure and Table: 4

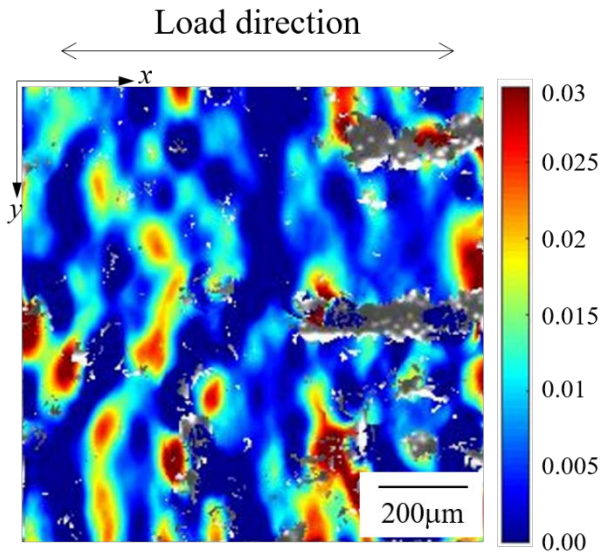

(a) ε_{xx}

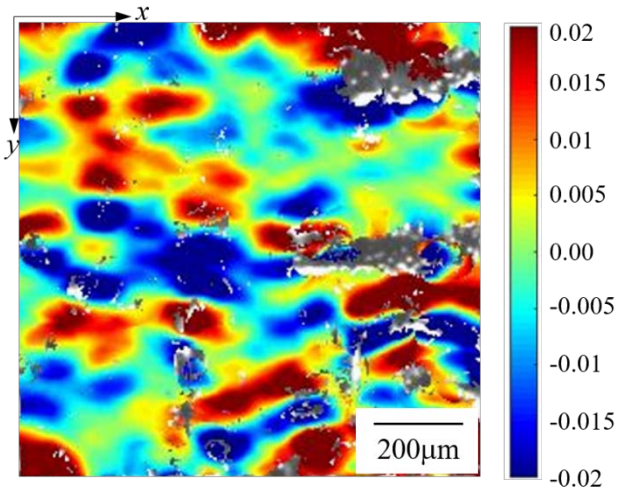

(b) ε_{yy}

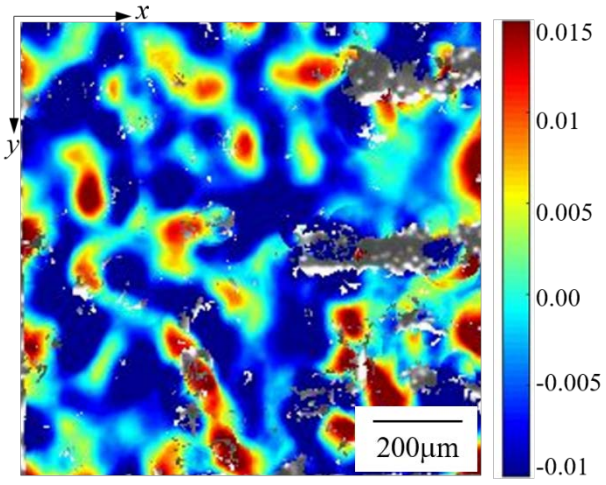

(c) $\gamma_{xy}/2$

Fig. 6 Strain distributions at 0 h.

Figure and Table: 5

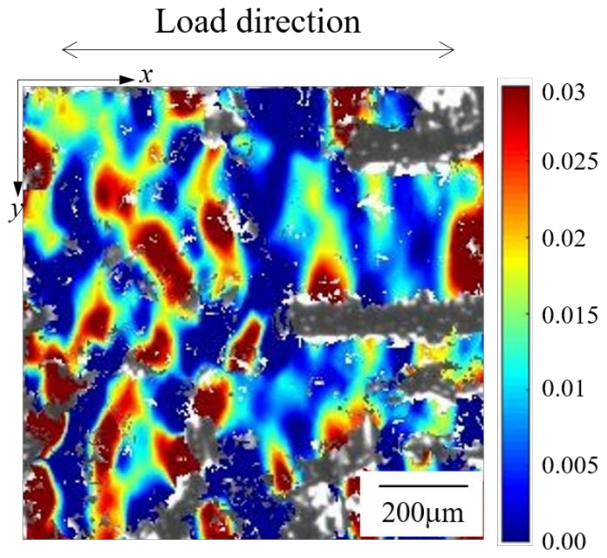

(a) ε_{xx}

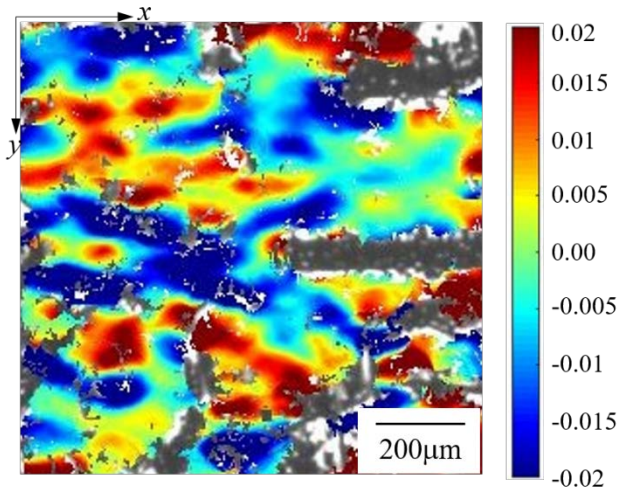

(b) ε_{yy}

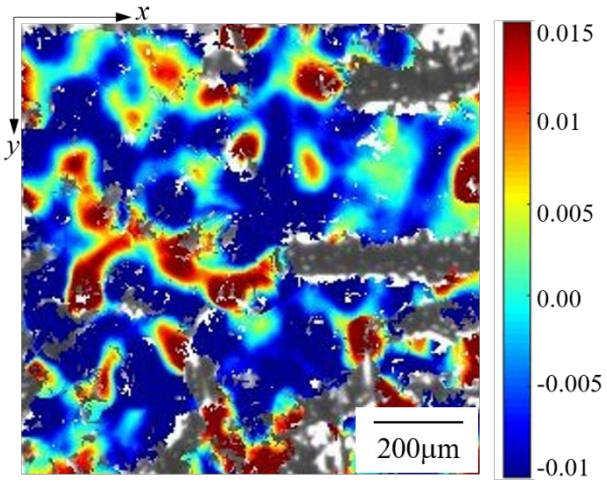

(c) $\gamma_{xy}/2$

Fig. 7 Strain distributions at 12 h.

Figure and Table: 6

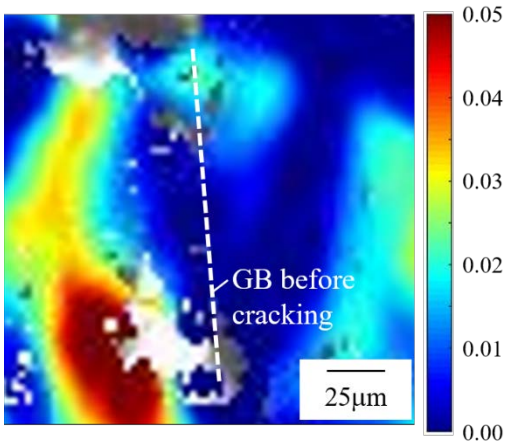

(a) 9 h

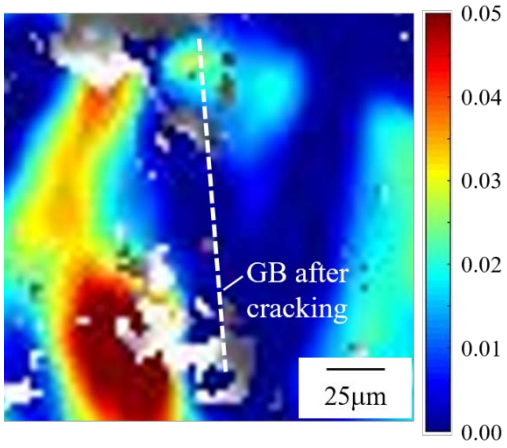

(b) 10 h

Fig. 8 Change in strain distribution around a cracked GB.

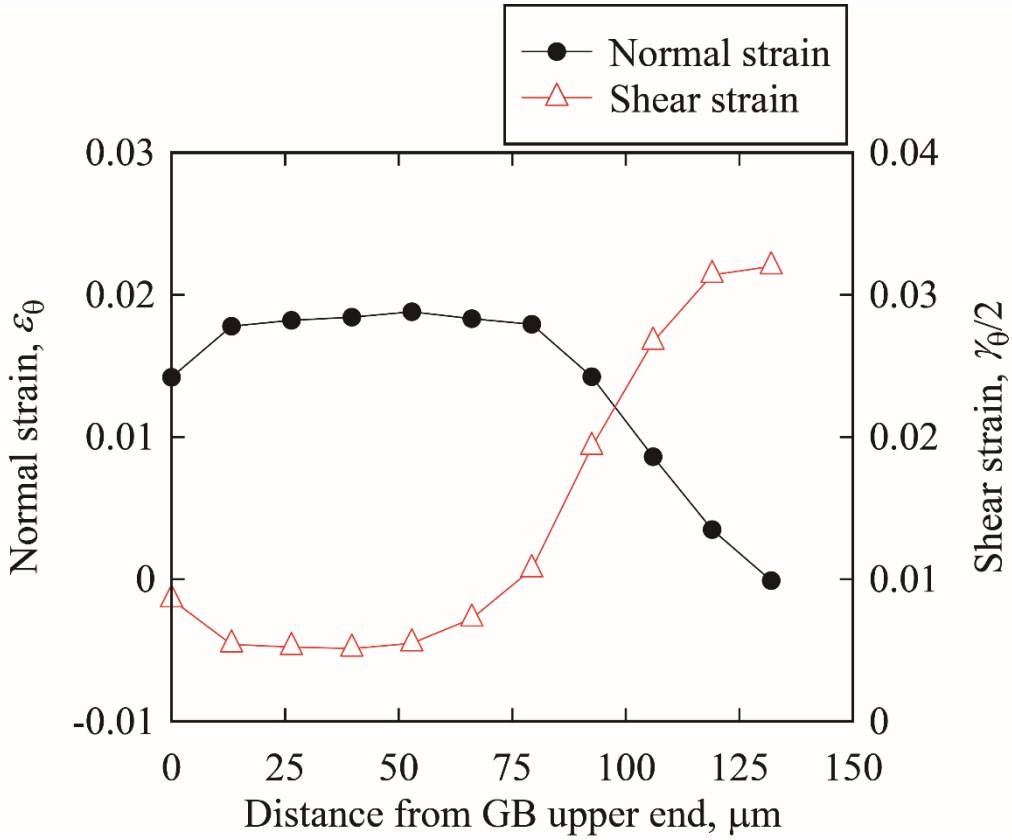

Fig. 9 Normal and shear strain distributions at a GB just before cracking.

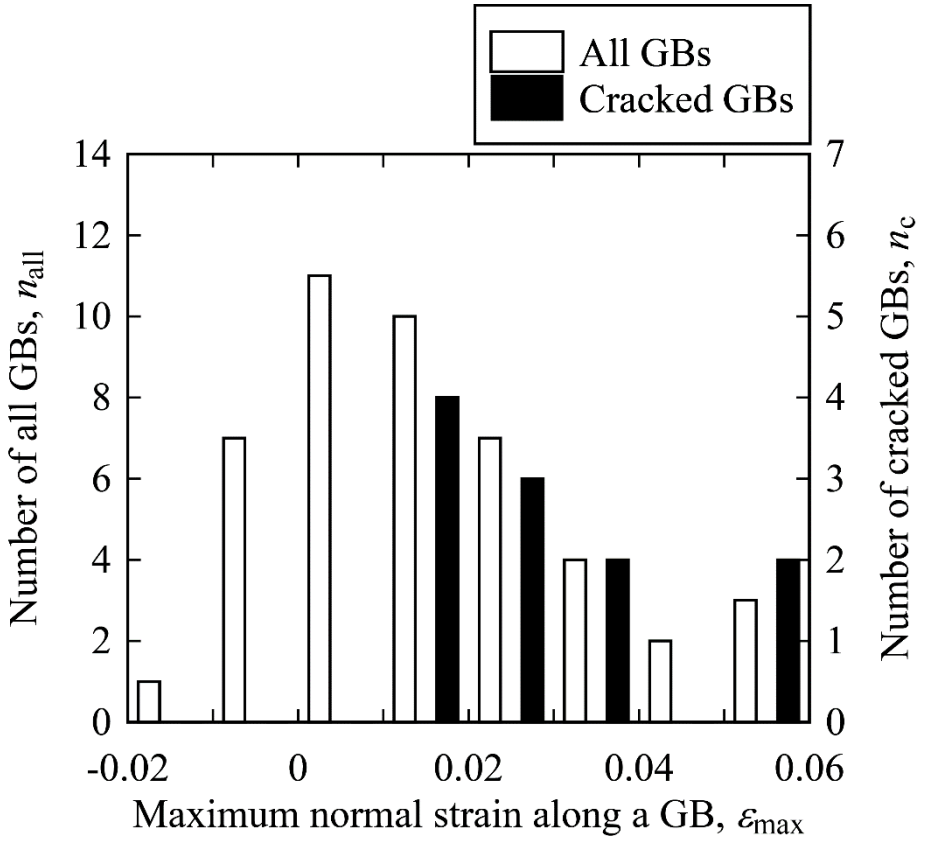

(a) Normal strain

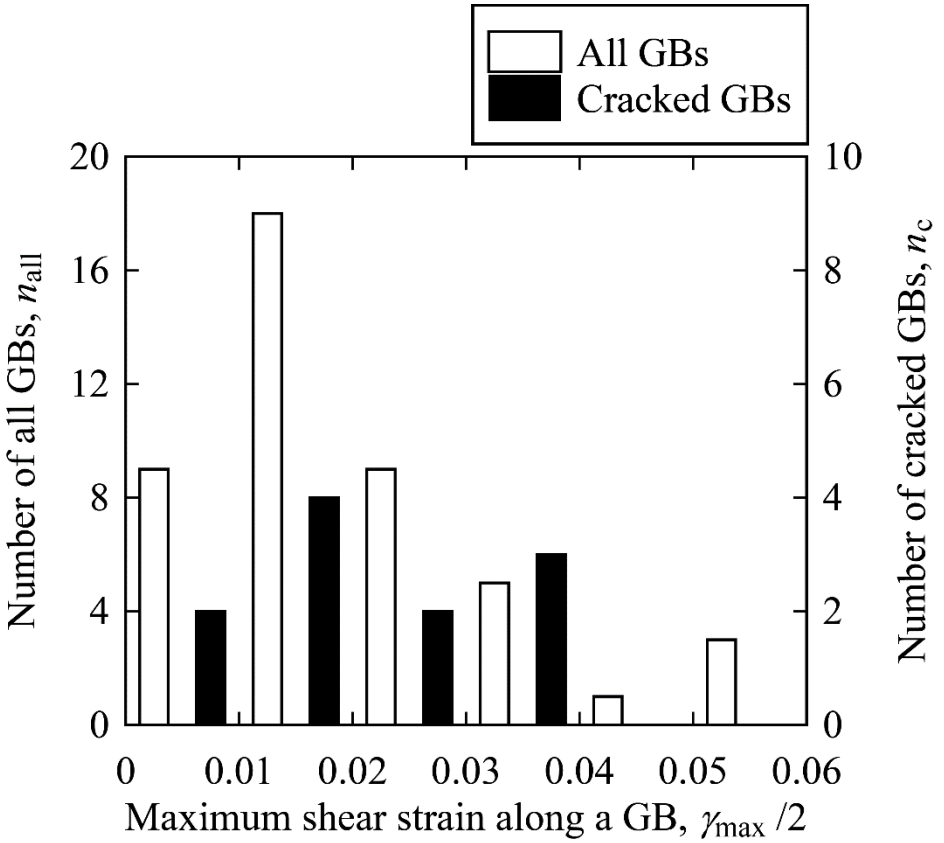

(b) Shear strain

Fig. 10 Histogram of the number of GBs versus strain.

Figure and Table: 9

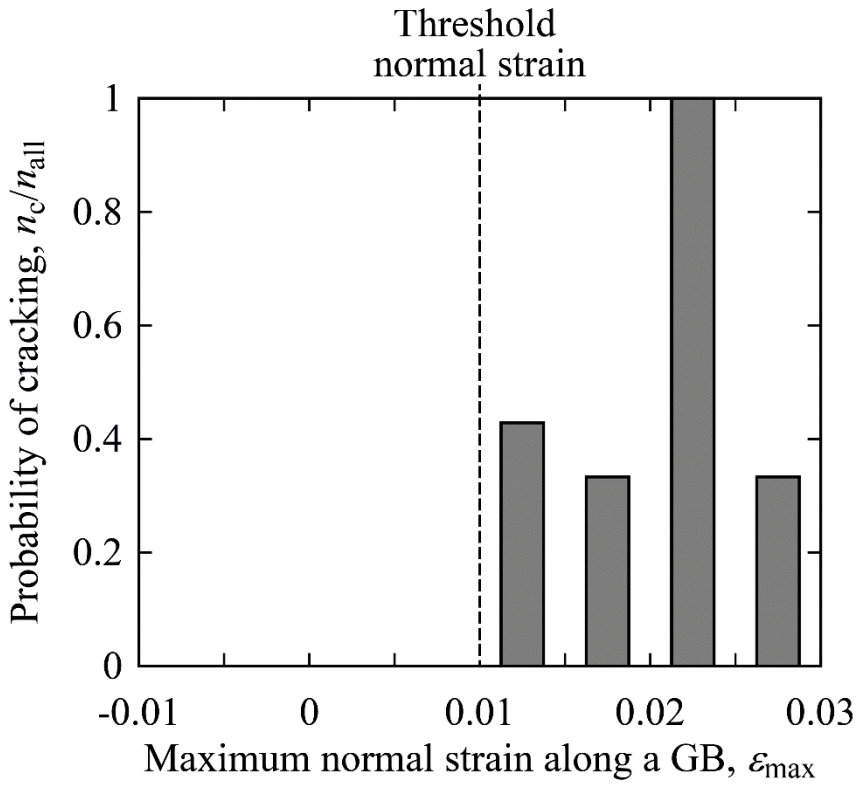

(a) Taking strain redistribution into account

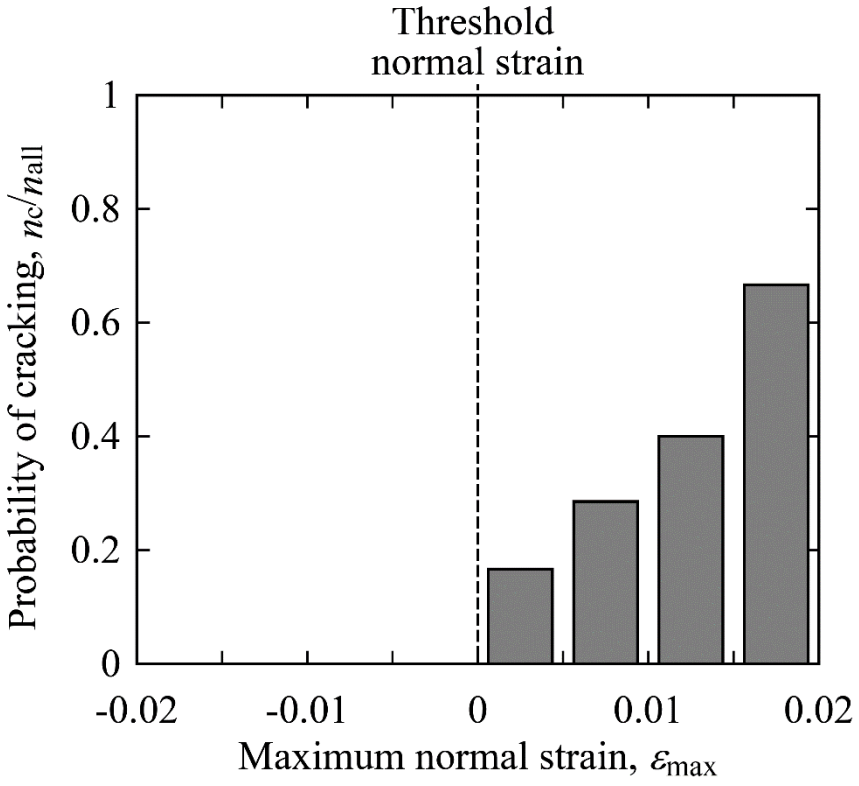

(b) Without taking strain redistribution into account [30]

Fig. 11 Histogram of probability of cracked GBs versus maximum normal strain.

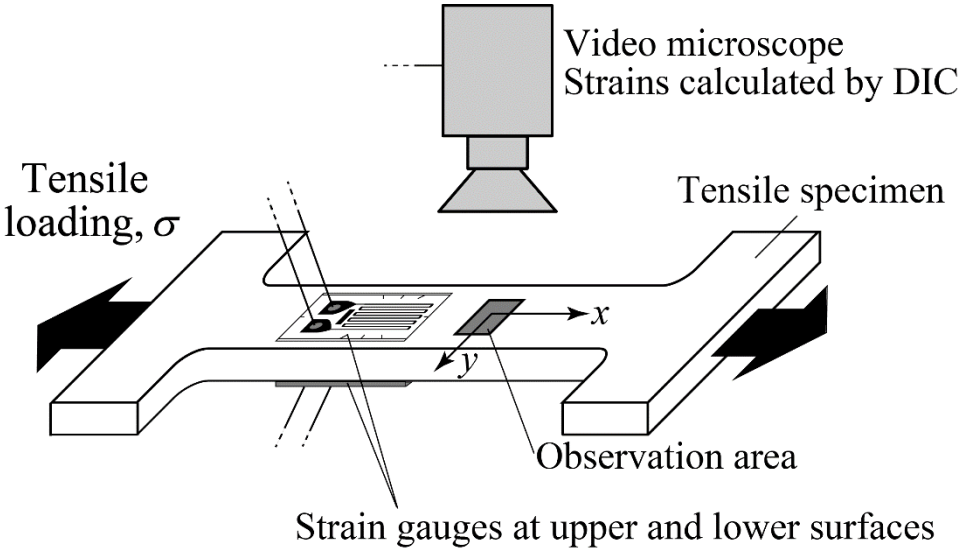

Fig. A.1 Schematic illustration of tensile testing.

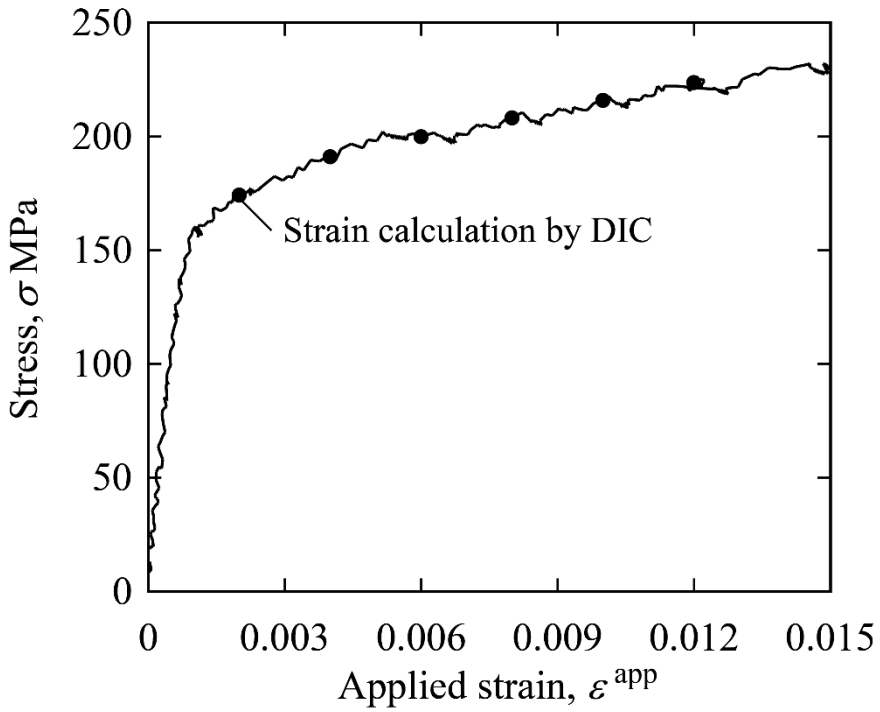

Fig. A. 2 Stress-strain curve and measurement condition of DIC

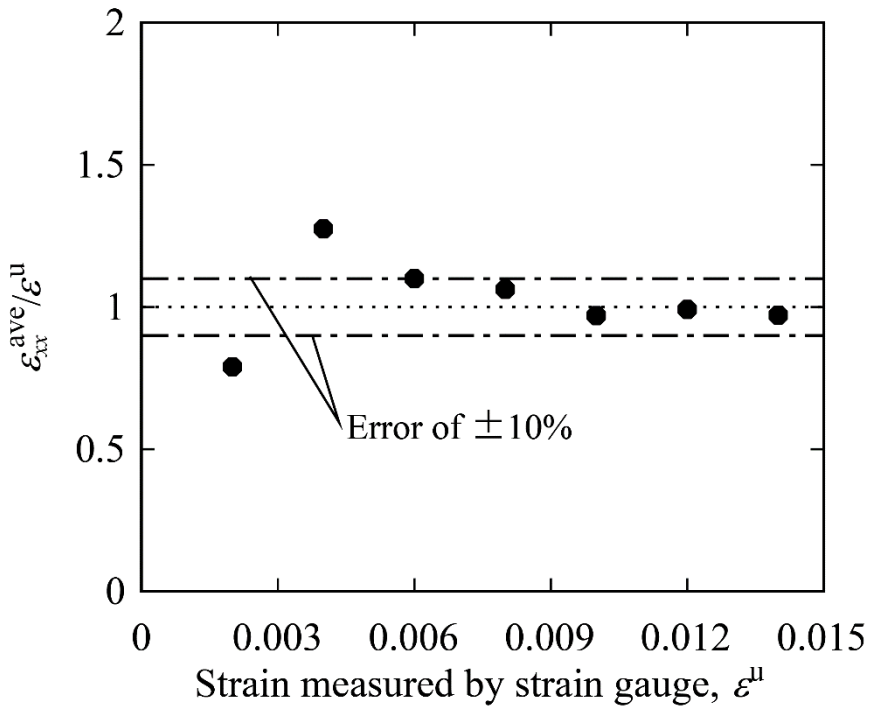

Fig. A. 3 Comparison of tensile strains measured by strain gauge and DIC.

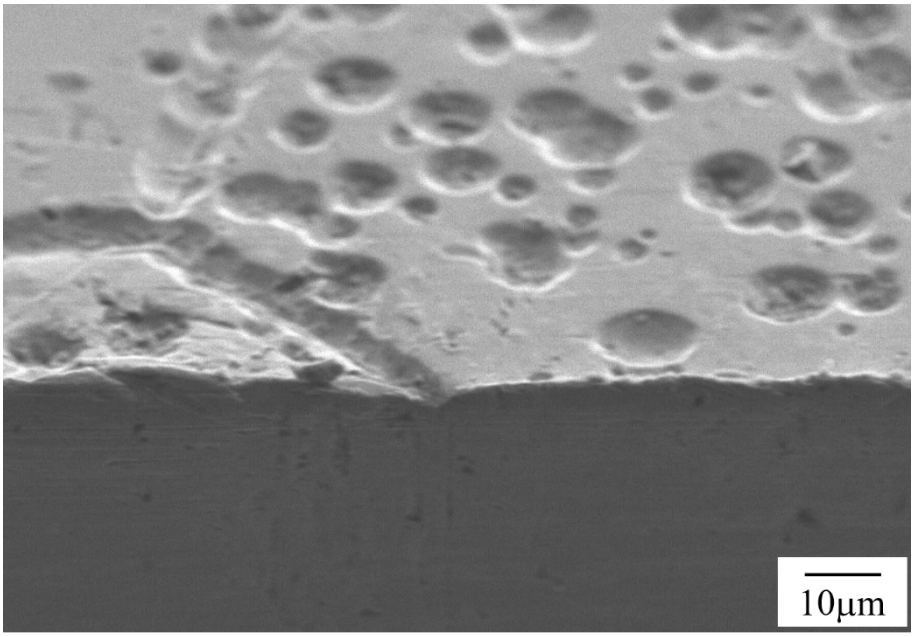

Fig. B.1 Details of a corrosion groove.

Tables

Table 1 Chemical composition (mass%) and mechanical properties of the steel used.

C	Si	Mn	P	S	Ni	Cr	Fe
0.06	0.47	0.87	0.03	0.003	8.05	18.16	Bal.

0.2% offset stress, MPa	Tensile strength, MPa	Elongation, %
206	520	40

Table 2 Conditions of strain measurement by DIC

Software	Ncorr
Strain	Euler-Almansi strain
Pixel resolution, μm	0.54
Subset sizes, pixel	91
Subset spacing, pixel	7
Observation area, pixel	1900 × 1900

Table B.1 Groove shape and strain concentration factors.

Depth, μm	2.5
Width, μm	6.6
Curvature radius, μm	8.5
K_T	2.1
K_ε	4.7